

# Long-Range Conformational Transition of a Photoswitchable Allosteric Protein: Molecular Dynamics Simulation Study

Sebastian Buchenberg,<sup>†</sup> Volker Knecht,<sup>†</sup> Reto Walser,<sup>‡</sup> Peter Hamm,<sup>‡</sup> and Gerhard Stock<sup>\*,†,§</sup>

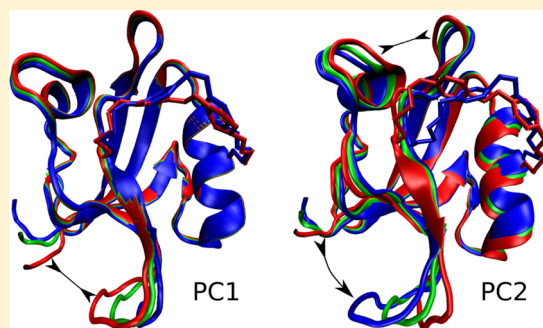
<sup>†</sup>Biomolecular Dynamics, Institute of Physics, University of Freiburg, 79104 Freiburg, Germany

<sup>‡</sup>Department of Chemistry, University of Zürich, CH-8057 Zürich, Switzerland

<sup>§</sup>Freiburg Institute for Advanced Studies (FRIAS), University of Freiburg, Albertstraße 19, 79104 Freiburg, Germany

## S Supporting Information

**ABSTRACT:** A local perturbation of a protein may lead to functional changes at some distal site. An example is the PDZ2 domain of human tyrosine phosphatase 1E, which shows an allosteric transition upon binding to a peptide ligand. Recently Buchli et al. presented a time-resolved study of this transition by covalently linking an azobenzene photoswitch across the binding groove and using a femtosecond laser pulse that triggers the cis–trans photoisomerization of azobenzene. To aid the interpretation of these experiments, in this work seven microsecond runs of all-atom molecular dynamics simulations each for the wild-type PDZ2 in the ligand-bound and -free state, as well as the photoswitchable protein (PDZ2S) in the cis and trans states of the photoswitch, in explicit water were conducted. First the theoretical model is validated by recalculating the available NMR data from the simulations. By comparing the results for PDZ2 and PDZ2S, it is analyzed to what extent the photoswitch indeed mimics the free-bound transition. A detailed description of the conformational rearrangement following the cis–trans photoisomerization of PDZ2S reveals a series of photoinduced structural changes that propagate from the anchor residues of the photoswitch via intermediate secondary structure segments to the C-terminus of PDZ2S. The changes of the conformational distribution of the C-terminal region is considered as the distal response of the isolated allosteric protein.



## INTRODUCTION

A local perturbation in a biological macromolecule may affect the function of distal sites of the molecule. This phenomenon denoted as allostery is central to many physiological processes.<sup>1,2</sup> The perturbation may be a binding event, post-translational modification, mutation, or light absorption. Traditionally, allostery has been interpreted in terms of structural changes<sup>3</sup> or shifts in the populations of alternative conformations.<sup>4</sup> More recently, it has been suggested that allostery may also be of dynamic origin with only marginal changes in average structure,<sup>5–9</sup> or that simultaneous changes in structure and dynamics play a significant role.<sup>10</sup> Driven by ongoing progress in experimental and theoretical methodology, there has been considerable effort to obtain a microscopic understanding of allosteric interactions and pathways.<sup>11–43</sup>

A well-studied example for systems showing ligand-induced allostery are modular domains for protein–protein interactions denoted as PSD95/Disks large/ZO-1 (PDZ) domains.<sup>11–20</sup> These domains occur in a set of proteins typically associated with cell junctions and mediate the clustering of membrane ion channels by binding to their C-termini.<sup>15–17</sup> PDZ domains share a common fold which consists of two  $\alpha$ -helices and six  $\beta$ -strands, with the second  $\alpha$ -helix and the second  $\beta$ -strand forming the canonical binding groove (Figure 1).<sup>18–20</sup> An example is the PDZ2 domain of human tyrosine phosphatase

1E, a protein involved in the regulation of multiple receptor-coupled signal transduction pathways, including programmed cell death.<sup>11</sup> Structural models of the PDZ2 domain based on experimental data suggest that the binding groove opens upon binding. That is, the  $C_{\alpha}$ -distance between residues 21 and 76 (green line in Figure 1) increases by 0.08 nm in crystals.<sup>16</sup> The nature of the subsequent ligand-induced intramolecular signaling process, however, remains a matter of debate, although various proposals of signaling pathways exist.<sup>30–38</sup>

To facilitate a dynamic perspective of the allosteric mechanism, recently Buchli et al.<sup>45</sup> presented a time-resolved study of the transition from the free to the bound state of PDZ2 triggered by a molecular photoswitch.<sup>46–51</sup> By covalently linking an azobenzene photoswitch across the binding groove and using a femtosecond laser pulse that affects the cis  $\rightarrow$  trans photoisomerization of azobenzene, they were able to initiate a conformational change similar to the free-bound transition. The photoswitch was attached at residues 21 and 76 of PDZ2 (Figure 1) because the  $C_{\alpha}$  distances between these anchor residues in the free and bound state closely match the linear extension of the photoswitch in the cis and trans states,

Received: July 10, 2014

Revised: November 3, 2014

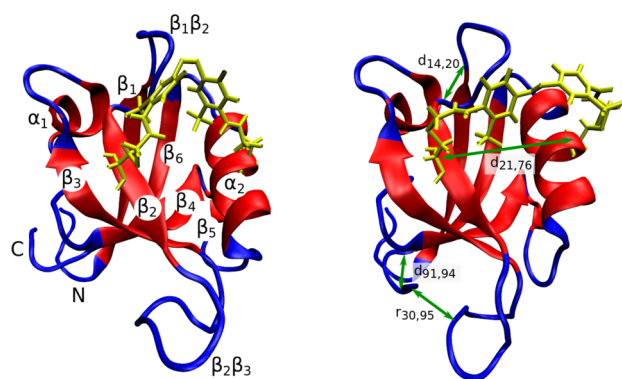


**Figure 1.** Structure of PDZ2S-cis (left) and PDZ2S-trans (right) as obtained from representative MD snapshots, respectively, showing  $\alpha$ -helices and  $\beta$ -sheets in red, loop regions in blue, and the azobenzene photoswitch including linker atoms in yellow. Labels in the left panel indicate the regions  $\beta_1$  (residues 6–12),  $\beta_2$  (20–23),  $\beta_3$  (35–40),  $\alpha_1$  (45–49),  $\beta_4$  (57–61),  $\beta_5$  (64–65),  $\alpha_2$  (73–80), and  $\beta_6$  (84–90). The most important loops connecting these regions are  $\beta_1$ – $\beta_2$  (13–19),  $\beta_2$ – $\beta_3$  (24–34),  $\beta_3$ – $\alpha_1$  (41–44), and  $\alpha_2$ – $\beta_6$  (81–83).<sup>44</sup> The green lines in the right panel indicate selected long-range distances which change significantly during the conformational transition following cis–trans photoisomerization of PDZ2S (see Figure 6).

respectively. In the remainder of the article, we refer to the photoswitchable protein as PDZ2S and to the wild-type system as PDZ2. Employing NMR spectroscopy and molecular dynamics simulations, Buchli et al. derived structural models of PDZ2S in the cis and trans states, which indicates that the  $C_\alpha$  distance between the anchor residues increases by about 0.2 nm upon switching from the cis to the trans state. Employing ultrafast vibrational spectroscopy, they showed that the conformational rearrangement of PDZ2S occurs in a highly nonexponential manner on various timescales from pico- to microseconds.

To aid the interpretation of the experimental results of Buchli et al., in this work we present a comprehensive molecular dynamics (MD) simulation study of PDZ2S. Starting from the NMR structures of PDZ2S in the cis or trans states, and PDZ2 in the ligand-free and -bound state, for each system seven microsecond runs of all-atom MD simulations in explicit water are performed and analyzed in detail. To validate the theoretical model, we first recalculate the available NMR data from the simulations. By comparing the results for PDZ2S and PDZ2, we then study possible effects of the photoswitch on the conformational distribution and dynamics of PDZ2, in order to analyze to what extent the photoswitch may mimic the free-bound transition. Finally, we focus on the conformational rearrangement following the cis–trans photoisomerization of the azobenzene photoswitch. We identify a series of photo-induced structural changes that propagate from the anchor residues of the photoswitch via intermediate secondary structure segments to the C-terminus of PDZ2S. The changes of the conformational distribution of the C-terminal region is considered as the distant structural response or the “allosteric response” of the isolated allosteric protein.

## METHODS

**Simulation Setup.** Using GROMACS with a hybrid GPU-CPU acceleration scheme,<sup>52</sup> PDZ2S-cis and PDZ2S-trans were simulated in aqueous NaCl solution for a total time scale of 7  $\mu$ s each. The protein was described using the Amber99sb\*-

ILDN<sup>53–55</sup> force field, the water by the TIP3P<sup>56</sup> model, and the ions with the model of ref 57. To obtain the force field parameters for the azobenzene photoswitch and the attached cysteine side chains, the structure of the switch and the side chains in the cis and the trans conformations was optimized on the B3LYP/6-31G\* level using the GAUSSIAN g09 program suite.<sup>58</sup> For both minimized structures, the electrostatic potential was computed using the Hartree–Fock method and the 6-31G\* basis set. For the multiconformational restrained electrostatic potential,<sup>59</sup> the  $C_\beta$  partial charges of the Cys residues were constrained to the value given in the Amber99sb\*-ILDN force field. To obtain the missing bond parameters for the sulfonate groups, the antechamber tool was employed.<sup>60</sup> The side chains of all four histidine residues (33, 54, 72, and 87) of PDZ2S were chosen electrostatically neutral (monoprotonated). The lengths of bonds involving hydrogens were constrained,<sup>61</sup> allowing for a 2 fs time step. Long-range electrostatic interactions were evaluated in reciprocal space using Particle-Mesh Ewald<sup>62</sup> with a maximum spacing for the FFT grid of 0.12 nm and an interpolation via a sixth-order polynomial. The minimal cutoff distance for electrostatic and van der Waals interactions was set to 1.2 nm. More details on the setup are provided in the Supporting Information.

The initial configuration of PDZ2S-cis and -trans were taken from Buchli et al.<sup>45</sup> (PDB entries 2M0Z and 2M10). Compared to the wild-type protein, PDZ2S contains an additional glycine residue at the N-terminus (residue 0), residues Ser-21 and Glu-76 were mutated into cysteines which are covalently attached to the azobenzene photoswitch, and two residues (Pro-95 and Thr-96) were appended at the C-terminus. The sequence of PDZ2S is given in Table S1 of the Supporting Information. Using periodic boundary conditions, the protein was placed into a dodecahedral box of linear size 5.8 nm filled with 4071 water molecules and one  $\text{Cl}^-$  ion to counterbalance the positive net charge of the protein. To mimic a salt concentration of 150 mM, according to the NMR and the IR experiments, 14  $\text{Na}^+$  and 14  $\text{Cl}^-$  ions were added. The system was relaxed to a local energy minimum using the steepest descent method. Subsequently, a 10 ns NPT simulation with harmonic restraints on the protein was conducted. The temperature of 300 K was maintained via the velocity rescaling algorithm<sup>63</sup> (0.1 ps relaxation time), and the pressure  $P = 1$  bar was controlled using the weak coupling method of Berendsen.<sup>64</sup> The final configuration was taken, and the box was scaled such that the box volume was equal to the average volume of the second half of the NPT simulation. Subsequently, the system was simulated for 1  $\mu$ s without harmonic restraints using an NVT ensemble. Finally a 1  $\mu$ s NVT production run was performed, saving atom coordinates every 20 ps. The configurations of this simulation at times 0–500 ns in steps of 100 ns and velocities drawn from Maxwell distributions were taken as initial conditions for six further NVT simulations. The initial 50 ns of these simulations were considered as a relaxation period and thus discarded. For comparison, also PDZ2 in the free state as well as binding the C-terminal peptide from the guanine nucleotide exchange factor RA-GEF-2 were simulated similarly, starting from structural models derived from X-ray crystallography (PDB entries 3LNX and 3LNY).<sup>16</sup>

**Analysis Methods.** Apart from various standard methods described in Results and Discussion, we used the following definitions for the analysis of the trajectories.

**Dihedral Angles.** Backbone dihedral angles  $\alpha = \phi, \psi, \chi$  of PDZ2S from the MD simulations were compared to

experimental values obtained from the program TALOS+,<sup>65</sup> which uses empirical relationships between chemical shifts and observed backbone dihedral angles. To avoid issues due to the periodicity of the dihedral angles, they were transformed according to  $x(\alpha) = \cos \alpha$  and  $y(\alpha) = \sin \alpha$ .<sup>66</sup> For both experimental and simulated dihedral angles, the average values of  $x(\alpha)$  and  $y(\alpha)$  were evaluated and the corresponding standard error was determined by block averaging, dissecting the set of trajectories into two distinct sets. In this way, we calculated for each backbone dihedral angle  $\alpha$ , the difference  $\Delta^2 = [x(\alpha_{\text{MD}}) - x(\alpha_{\text{exp}})]^2 + [y(\alpha_{\text{MD}}) - y(\alpha_{\text{exp}})]^2$  and determined the standard error  $d\Delta^2$  via error propagation. A backbone dihedral angle was considered to deviate from experiment if  $\Delta^2 > d\Delta^2$ .

**NOE Distances.** To obtain NOE distances  $R_{ij}$  between two atoms  $i$  and  $j$  from the MD simulations, we calculated for each of the trajectories the quantity  $R_{ij,k}^{-6} = \langle r_{ij}^{-6} \rangle_k$ , where  $k = 1, \dots, 7$  labels the individual trajectories and the average goes over all frames of the trajectory as well as over atoms that cannot be distinguished in these experiments (see the Supporting Information). We next computed the mean  $R_{ij}^{-6} = 1/7 \sum_{k=1,7} R_{ij,k}^{-6}$  and the standard error  $\sigma_{ij}^{-6}$  of this mean. The statistical error of the NOE distances  $R_{ij}$  is derived via error propagation as  $\sigma_{ij} = \sigma_{ij}^{-6} (R_{ij}^{-6})^{-7/6}$ . A given NOE distance was considered to be violated if the calculated lower bound  $R_{ij}^{\text{low}} = R_{ij} - \sigma_{ij}$  is larger than the experimental upper bound  $R_{ij}^{\text{exp}}$ .

**Secondary Structure.** The definition of secondary structure content is based on the existence of hydrogen (H) bonds within the protein's main chain using DSSP<sup>67</sup> with an energy cutoff criterion according to the following definitions. An  $n$ -turn is characterized by a H bond between residues  $i$  and  $i + n$ . Two or more consecutive  $n$ -turns form an  $n$ -helix. The case,  $n = 4$  indicates an  $\alpha$ -helix and  $n = 3$  a  $3_{10}$ -helix. Two strands joined by H bonds involving alternating residues on each participating strand indicate a  $\beta$ -sheet if each strand contains at least two residues.

**Residue–Residue Contacts.** For each pair of residues  $i \neq j$ , the distance  $r_{ij}$  was defined as the minimal distance between any atom of  $i$  and any atom of  $j$ . If  $r_{ij} < 0.45$  nm, the residues were considered to be in contact. Denoting the contact probability of residues  $i$  and  $j$  by  $P_{ij}$ , the change  $\Delta P_{ij} = P_{ij}^{\text{trans}} - P_{ij}^{\text{cis}}$  upon cis-trans photoisomerization was calculated and listed in Table 1 if  $|\Delta P_{ij}| \geq 0.3$ .

**Hydrogen Bonds.** As usual, a H bond was considered to be formed if the donor–acceptor distance is below 0.36 nm and the hydrogen-donor–acceptor angle is below 35°.

## RESULTS AND DISCUSSION

**1. Comparison to Experiment. RMSD.** Figure 2 shows the distribution of root-mean-square deviations (rmsd) of configurations of PDZ2S-cis and -trans with respect to the corresponding NMR structures,<sup>45</sup> as well as the rmsd of configurations of PDZ2-free and -bound with respect to the corresponding X-ray structures.<sup>16</sup> PDZ2-free shows a bimodal distribution, indicating (at least) two conformational substates. The average rmsd is  $(0.16 \pm 0.01)$  nm for PDZ2-free,  $(0.14 \pm 0.01)$  nm for PDZ2-bound,  $(0.29 \pm 0.01)$  nm for PDZ2S-cis, and  $(0.30 \pm 0.02)$  nm for PDZ2S-trans. The average rmsd of PDZ2 in the free and bound state are comparable to the resolution of the corresponding X-ray experiments, which were 0.164 nm for the free state and 0.130 nm for the bound state,<sup>16</sup> giving some confidence in the reliability of these simulations. The average rmsd of PDZ2S, on the other hand, are 2-fold larger than the corresponding average rmsd of PDZ2, indicating

**Table 1. Contacts between Residue  $i$  in Segment  $S_i$  and Residue  $j$  in Segment  $S_j$  that Change Significantly ( $\Delta P_{ij} \geq 0.3$ ) upon Cis–Trans Isomerization of PDZ2S, where  $\Delta P_{ij} = P_{ij}^{\text{trans}} - P_{ij}^{\text{cis}}$  Denotes the Change of the Contact Probability<sup>a</sup>**

$S_i$	$S_j$	$i$	$j$	$\Delta P$	type
$\alpha_2$	$\alpha_2$	Gln-73	Thr-77	0.31	HB <sub>mc</sub>
$\alpha_2$	$\alpha_2$	Ala-74	Leu-78	0.41	HB <sub>mc</sub>
$\alpha_2$	$\alpha_2$	Val-75	Arg-79	0.40	HB <sub>mc</sub>
$\alpha_2$	$\alpha_2$	Val-75	Leu-78	−0.42	HB <sub>mc</sub>
$\alpha_2$	$\beta_1\text{--}\beta_2$	Cys-76	Ser-17	−0.34	—
$\alpha_2$	$\beta_1\text{--}\beta_2$	Leu-78	Lys-13	−0.40	—
$\alpha_2$	$\beta_1\text{--}\beta_2$	Leu-78	Leu-18	−0.39	np
$\alpha_2$	$\beta_2$	Val-75	Val-22	−0.32	np
$\alpha_2$	$\beta_2$	Arg-79	Cys-21	0.64	—
$\alpha_2$	$\beta_3$	Ala-74	Ile-35	0.37	np
$\alpha_2$	$\beta_3$	Leu-78	Ile-35	0.50	np
$\alpha_2$	$\beta_3$	Thr-77	Val-64	0.31	—
$\alpha_2$	$\beta_6$	Leu-78	Val-85	−0.33	np
$\alpha_2$	$\beta_5\text{--}\alpha_2$	Gln-73	Ala-69	0.35	—
$\alpha_2$	$\beta_5\text{--}\alpha_2$	Ala-74	Ala-69	0.30	np
$\alpha_2$	$\beta_5\text{--}\alpha_2$	Val-75	Leu-66	−0.34	np
$\alpha_2$	$\beta_5\text{--}\alpha_2$	Thr-77	Leu-66	0.50	—
$\beta_5\text{--}\alpha_2$	$\beta_5$	Gly-68	Ser-65	0.41	HB <sub>sc</sub>
$\beta_6$	C	Glu-90	Gln-93	0.38	—
$\beta_1\text{--}\beta_2$	$\beta_1\text{--}\beta_2$	Lys-13	Asp-15	−0.38	—
$\beta_1\text{--}\beta_2$	$\beta_1\text{--}\beta_2$	Lys-13	Ser-17	0.32	—
$\beta_1\text{--}\beta_2$	$\beta_1\text{--}\beta_2$	Asn-14	Ser-17	0.42	HB <sub>mc</sub>
$\beta_1\text{--}\beta_2$	$\alpha_2\text{--}\beta_6$	Asn-14	Gln-83	−0.40	—
$\beta_2\text{--}\beta_3$	$\beta_2\text{--}\beta_3$	Gly-24	Gly-34	−0.32	—
$\beta_2\text{--}\beta_3$	$\beta_5\text{--}\alpha_2$	His-32	Glu-67	0.32	—
$\beta_2\text{--}\beta_3$	C	Val-30	Ser-94	0.38	—
$\beta_2\text{--}\beta_3$	C	Val-30	Pro-95	0.31	—
$\beta_3$	$\beta_5\text{--}\alpha_2$	Ile-35	Ala-69	−0.41	np
$\beta_3$	$\beta_5\text{--}\alpha_2$	Ile-35	Thr-70	−0.39	—
$\beta_3$	C	Tyr-36	Ser-94	0.43	—
$\alpha_1\text{--}\beta_4$	C	Gly-55	Gln-93	0.34	—
$\alpha_1\text{--}\beta_4$	C	Gly-55	Ser-94	0.44	—
$\beta_4$	$\beta_5\text{--}\alpha_2$	Arg-57	Glu-67	0.34	—
$\beta_4$	$\alpha_2\text{--}\beta_6$	Val-61	Thr-81	0.35	—

<sup>a</sup>Here  $P_{ij}^{\text{cis}}$  or  $P_{ij}^{\text{trans}}$  denote the probability that the minimal distance between residue  $i$  and  $j$  in PDZ2S-cis or -trans, respectively, is below 0.45 nm. The last column indicates whether a given contact is a H bond within the main chain (HB<sub>mc</sub>), a H bond between the main and a side chain (HB<sub>sc</sub>), or a contact between two hydrophobic residues (np). In line with the discussion, the upper part of the table describes contact changes at the  $\alpha_2$  side and the lower part changes at the  $\beta_2$  side of the binding pocket.

significant deviations from the structural models inferred from the experiment. As an illustration, Figure S1 of the Supporting Information shows the time evolution of the rmsd of PDZ2S, which reveals that some parts of the trajectories (e.g., simulation 1 of the cis state after 850 ns) sample regions of phase space that are not populated by the other MD runs. In fact, it has been discussed that, compared to X-ray crystallography, NMR-derived structures have on average higher internal strain and are more likely to diverge in MD simulations.<sup>68</sup>

**Conformational Distribution.** To obtain a global view of the structural distribution of PDZ2S from the MD simulations and the NMR models, we performed a principal component analysis (PCA) on the  $C_\alpha$  atoms.<sup>69</sup> The corresponding covariance matrix was determined from the merged simulation



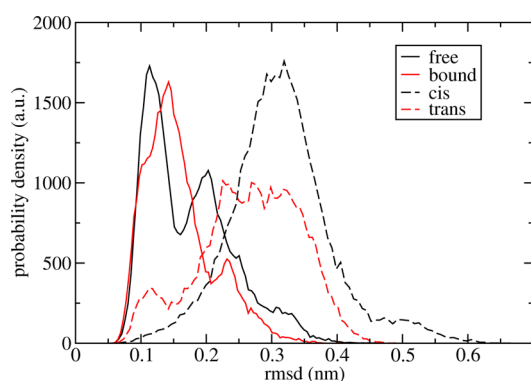


**Figure 2.** Calculated distributions of the rmsd of PDZ2 in its free and bound state as well as of PDZ2S in its cis and trans states.

trajectories of the cis and the trans states. To ensure that this strategy results in well-defined reaction coordinates, we have also performed separate PCAs on the cis and trans trajectories, respectively (see the discussion of Figure S12 of the Supporting Information). With the use of the two principal components with the largest variance, PC1 and PC2, Figure 3 (top) shows

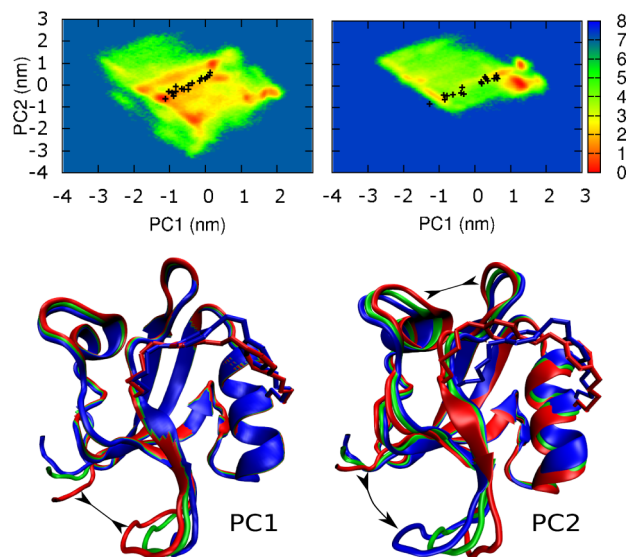


**Figure 3.** (Top) Free energy (in units of  $k_B T$ ) as a function of PC1 and PC2 from a principal component analysis on the  $C_\alpha$  atoms on the merged trajectories of PDZ2S-cis and PDZ2S-trans, shown for (left) the cis and (right) the trans states. The positions of the respective NMR structures are indicated by black crosses. (Bottom) Structural evolution along PC1 and PC2, showing the protein in ribbon representation and the azobenzene switch, including linkers in stick representation. The colors distinguish between three different structures along the respective PC.

the resulting free-energy landscape of PDZ2S-cis and PDZ2S-trans. The cis and trans states are seen to exhibit seven and three prominent minima, respectively. The overall population of these regions with free energies below  $2 k_B T$  is 55% for the cis and 48% for the trans state. The conformational rearrangements associated with the first few PCs mainly account for structural changes of the flexible loops (particularly  $\beta_1$ - $\beta_2$  and  $\beta_2$ - $\beta_3$ ), which in turn affects an overall spatial rearrangement of the  $\beta$ -sheets and  $\alpha$ -helices of PDZ2S, see Figure 3 (bottom). Specifically, PC1 accounts for the motion of the  $\beta_2$ - $\beta_3$  loop toward the C-terminal loop, while PC2 reflects the motion of

the  $\beta_1$ - $\beta_2$  loop toward the  $\alpha_1$ -helix and the opening of the binding groove.

For comparison, the position of the NMR structures with lowest energy is indicated. The reason for their much narrower structural distribution is presumably that the NMR structures are motionally averaged to a certain extent, with the NMR observables like NOE distances applied as instantaneous restraints to picosecond MD simulations. This is by far not as sophisticated as sampling configurational space using microsecond MD simulations as done in the present work. A much more stringent comparison between simulation and experiment is therefore obtained, if one directly calculates NMR observables (backbone dihedral angles and NOE distances) from the MD trajectories.

**Backbone Dihedral Angles.** Among the 73 residues for which experimental TALOS+ estimates for backbone dihedral angles were available, deviations from the experiment were observed for 2 residues (3%) in the cis and 4 residues (5%) in the trans state (see Methods). In the cis state, deviations are seen for residues Cys-21 and Val-26 ( $\beta_2$  region), in the trans state, residues Lys-13 ( $\beta_1$  region), Glu-67 and Gly-68 ( $\beta_5$ - $\alpha_2$  loop), and Cys-76 ( $\alpha_2$ -region) differ from those of the experiment. These cases are described in Table S2 of the Supporting Information and their Ramachandran plots from the simulations are shown in Figure S3 of the Supporting Information. The latter reveal that residues exhibiting deviations show an equilibrium between multiple secondary structure motifs. This is in contrast to the assumption underlying the experimental assignment that only a single motif applies, which limits the significance of these experimental results.

**NOE Distances.** The most important NOE distances are those between residues  $i$  and  $j$  with  $j > i + 3$ , which we denote as long-range NOEs. The NMR experiments provided 877 NOEs (including 289 long-range NOEs) for PDZ2S-cis and 992 NOEs (including 316 long-range NOEs) for PDZ-trans. The MD simulations violated 8% of all and 9% of the long-range NOEs for PDZ2S-cis, and 8% of all and 10% of the long-range NOEs for PDZ-trans. The violated long-range NOEs, 28 for cis and 34 for trans, are listed in Tables S3 and S4 of the Supporting Information. They correspond to an average distance deviation of  $0.04(\pm 0.04)$  nm for cis and  $0.07(\pm 0.04)$  nm for trans. Seven of these violations involved Ala-60, whose NMR peak strongly overlapped with that for Thr-96. Moreover, 24 violations involved residues close to the very flexible C-terminal region ( $N \geq 88$ ).

**Secondary Structure.** It is interesting to what extent the overall good agreement between experimental and simulated NMR data is reflected in the predicted secondary structure of PDZ2S. Figure S4 of the Supporting Information compares the fraction of  $\beta$ -sheet and  $\alpha$ -helical conformations of the individual residues (see Methods for definition) for PDZ2S-cis and PDZ2S-trans, as obtained from the simulations and the structural models derived from the NMR data. In the NMR structures, the  $\beta$ -sheet conformations in regions  $\beta_1$  to  $\beta_4$  and  $\beta_6$  as well as  $\alpha$ -helical conformations in regions  $\alpha_1$  and  $\alpha_2$  are present in 100% and  $\beta$ -sheet conformations of the  $\beta_5$  region are present in 80% of the structures. In the MD simulations,  $\beta$ -sheet conformations are present in 100% of the configurations in regions  $\beta_1$  and  $\beta_{4-6}$ , while they are somewhat destabilized in regions  $\beta_2$  and  $\beta_3$ . Residues in  $\alpha_1$  feature 60%  $\alpha$ -helical structures. In  $\alpha_2$ , we have 60%  $\alpha$ -helical and 10–40%  $3_{10}$ -helical

conformations for PDZ2S-cis and 100%  $\alpha$ -helical conformations for PDZ2S-trans.

## 2. Effect of the Photoswitch on the PDZ2 Domain.

**Rmsd and Rmsf.** Next we wish to investigate to what extent the photoinduced conformational rearrangement in PDZ2S mimics the ligand-induced conformational change in wild-type PDZ2. The distributions of the rmsd pertaining to PDZ2S and PDZ2 shown in Figure 2 already indicated that the conformational distribution of PDZ2S is considerably more heterogeneous as in the case of PDZ2. Given that the variance of the rmsd is significantly larger for PDZ2S than for PDZ2, at first sight, the photoswitch apparently leads to some destabilization of the protein. Assuming that our simulations only sample the folded state of both PDZ2S and PDZ2, though, the higher flexibility of PDZ2S versus PDZ2 observed in our simulations might indicate that the folded state of PDZ2S has a higher entropy than the folded state of PDZ2. In addition, the cross-link between residues 21 and 76 for PDZ2S is expected to decrease the entropy of the unfolded state of PDZ2S compared to the unfolded state of PDZ2. Both effects would imply an entropic stabilization of the folded state for PDZ2S versus PDZ2. A slight stabilization of the folded state for PDZ2S compared to PDZ2 is indeed suggested from experiments by CD spectroscopy, revealing that the melting temperature is higher for the photoswitched system (44 °C for PDZ2S-cis and 42 °C for PDZ2S-trans) than for the wild-type system (38 °C for free PDZ2).<sup>70</sup>

A similar picture is obtained from the root-mean-square fluctuations (rmsf) of the  $C_\alpha$  atoms for PDZ2-free and -bound as well as PDZ2S-cis and -trans (Figure 4). As expected, the

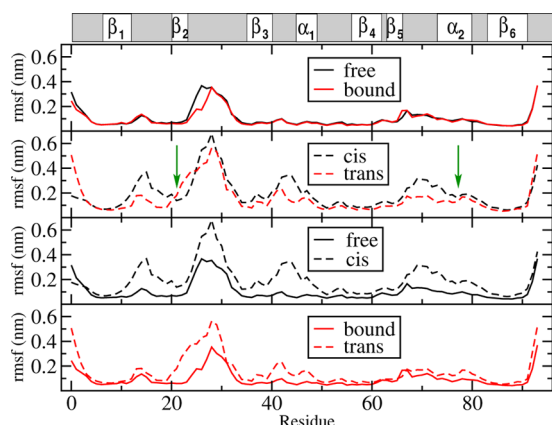


**Figure 4.** Root mean square fluctuations of the  $C_\alpha$  atoms of PDZ2 in its free and bound states and of PDZ2S in its cis and trans states. The green arrows at position 21 and 76 indicate the anchor residues of the photoswitch.

photoswitched systems show enhanced fluctuations of the terminal residues as well as in the various loops. Ligand binding of the wild-type system hardly changes the  $C_\alpha$  fluctuations, except that the rmsf of the  $\beta_2$ - $\beta_3$  loop become somewhat smaller. Upon attachment of the photoswitch at residues 21 and 76, the overall rmsf increase by roughly a factor of 2. In particular, the loops  $\beta_1$ - $\beta_2$ ,  $\beta_2$ - $\beta_3$ ,  $\beta_3$ - $\alpha_1$ , and  $\beta_5$ - $\alpha_2$  are found to exhibit elevated flexibility. Notably, the rmsf of PDZ2-bound and PDZ2S-trans are more similar than are the rmsf of PDZ2-free and PDZ2S-cis. This indicates that PDZ2S-trans is closer to the wild-type system than PDZ2S-cis.

**Secondary Structure.** To compare the secondary structure of the wild-type and the photoswitchable protein, Figure 5

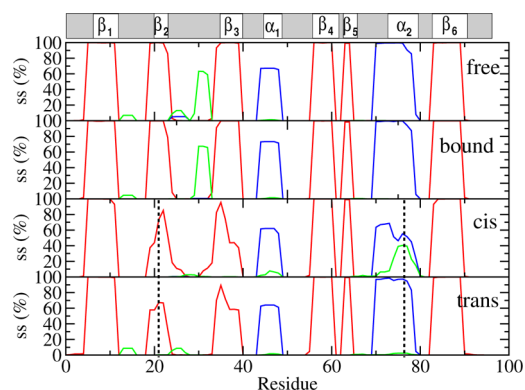


**Figure 5.** Secondary structure of (from top to bottom) PDZ2 in free and bound, as well as PDZ2S domain in the cis and trans states. Shown is the content of  $\beta$ -sheet (red),  $\alpha$ -helical (blue), and  $3_{10}$ -helical conformations (green) of the individual residues as obtained by DSSP. The dashed lines at position 21 and 76 indicate the anchor residues of the photoswitch.

shows the content of  $\beta$ -sheet and  $\alpha$ -helical conformations of the individual residues as obtained by DSSP (see Methods). In the wild-type system, all  $\beta$ -sheets ( $\beta_1$  to  $\beta_6$ ) and the  $\alpha_2$ -helix are completely stable, the  $\alpha_1$ -helix is found 60% of the time, and some  $3_{10}$ -helical structures occur in the  $\beta_1$ - $\beta_2$  loop. The attachment of the photoswitch at residues 21 and 76 leads to a destabilization of the  $\beta$ -sheets,  $\beta_2$  and  $\beta_3$ . In PDZ2S-cis, moreover, the  $\alpha_2$ -region is somewhat destabilized and also shows some  $3_{10}$ -helical structures. This is a consequence of the fact that in PDZ2S-cis, the photoswitch tightly restrains the width of the binding pocket, significantly more than in the wild-type unbound PDZ2.

**Tertiary Structure.** As discussed below, the main structural change associated with the conformational transition in PDZ2S is reflected in the overall spatial rearrangement of its  $\beta$ -sheets and  $\alpha$ -helices. These changes in tertiary structure can be monitored through long-range distances between the secondary structure elements. As an example, we consider the distribution of representative distances between remote residues, which change significantly during the free-bound transition of PDZ2 (Figure S5 of the Supporting Information) and the cis–trans transition of PDZ2S (Figure 6), respectively. The distances monitor conformational changes starting with the binding site, via intermediate secondary structure elements, to the C-terminus, see Discussion below. In general, the structural changes in the wild-type system are more subtle than the more substantial changes in PDZ2S, particularly in the vicinity of the photoswitch.

**3. Characterization of the Conformational Rearrangement.** We now focus on the conformational transition of PDZ2S subsequent to cis–trans photoisomerization. To this end, we first recall some main findings made above. Figure 3 revealed that the conformational distribution in PDZ2S-cis is significantly more heterogeneous than in PDZ2S-trans. This is in line with the observation that PDZ2S-cis exhibits larger fluctuations than PDZ2S-trans (Figure 4) and that the  $\alpha_2$ -helix is more stable in PDZ2S-trans (Figure 5). As discussed in the following, this overall stabilization of PDZ2S-trans compared to PDZ2S-cis is a consequence of changing residue–residue contacts and H bonds, which are listed in Table 1. Moreover,

the conformational rearrangement is characterized by changes of the backbone dihedral angles (Table S5 and Figures S6–S11 of the Supporting Information) and the long-range distance distributions shown in Figure 6.

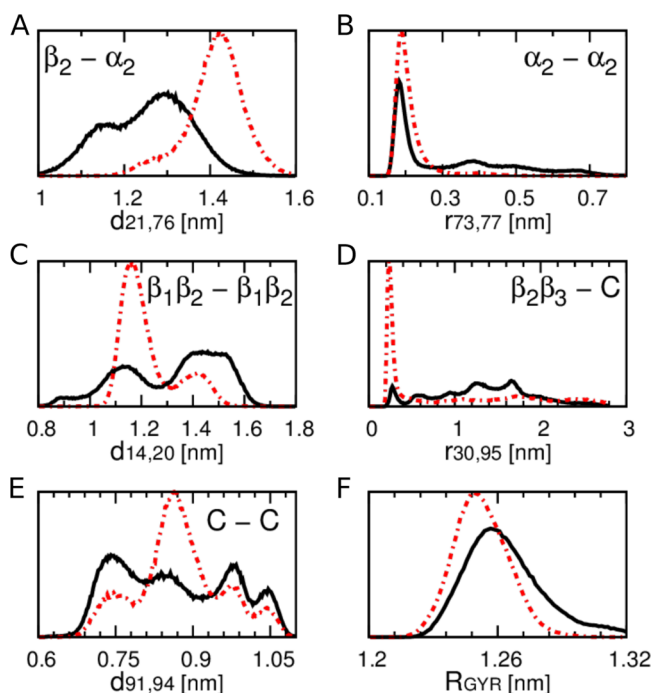


**Figure 6.** Various distance distributions that change significantly as a consequence of the photoisomerization of PDZ2S from cis (black curves) to trans (red curves). (A) The opening of the binding pocket is monitored by the  $C_{\alpha}$ -distance  $d_{21,76}$  between the anchor residues Cys-21 and Cys-76 of the photoswitch. (B) At the Cys-76 end, we find a stabilization of the  $\alpha_2$ -helix via the formation of three  $(n,n+4)$  H bonds, which is exemplified by the distribution of the minimum distance between Gln-73 and Thr-77. (C) At the Cys-21 end, we observe a compacting of the  $\beta_1$ - $\beta_2$  loop, monitored by its end-to-end  $C_{\alpha}$ -distance  $d_{14,20}$ . (D) The allosteric response at the C-terminal region can be characterized by the formation of two contacts between the C-terminal loop and the  $\beta_1$ - $\beta_2$  loop, exemplified by the minimum distance between residues Val-30 and Pro-95. (E) Moreover, we observe a significant change of the conformational distribution of the C-terminal loop, monitored by its end-to-end distance  $d_{91,94}$ . (F) In total, the conformational transition affects an overall compacting of PDZ2S-trans compared to PDZ2S-cis, which is revealed by the corresponding distributions of the radius of gyration.

On the basis of the structural differences between PDZ2S-cis and PDZ2S-trans and their sequential and spatial distance to the photoswitch, a series of photoinduced structural changes may be inferred. As the azobenzene photoswitch is attached to the side chains of Cys-21 (in the  $\beta_2$ -strand) and Cys-76 (in the  $\alpha_2$ -helix), we describe the induced structural changes starting from these two anchor residues. Initially, the cis–trans photoisomerization opens the binding pocket of PDZ2S, as is nicely seen from the shift of the corresponding  $C_{\alpha}$ -distance  $d_{21,76}$  in Figure 6A. We note that the distribution of  $d_{21,76}$  is significantly narrower in PDZ2S-trans than in PDZ2S-cis. This is another manifestation of the fact that PDZ2S-cis shows numerous coexisting conformational states, while PDZ2S-trans exhibits a much smaller structural heterogeneity (Figure 3).

As Cys-76 is located in the middle of the  $\alpha_2$ -helix, the photoinduced structural changes of Cys-76 foremost leads to a

rearrangement of  $\alpha_2$ . That is, the  $\alpha_2$ -helix gains three  $(n,n+4)$  H bonds while loosing an  $(n,n+3)$  H bond, which leads to a stabilization of the  $\alpha$ -helix at the expense of  $3_{10}$ -helical conformations (Table 1). As an example, the formation of the H bond between Gln-73 and Thr-77 is illustrated in Figure 6B, that shows the change of the distance distribution between these residues. Table 1 lists 13 further contact changes involving  $\alpha_2$ . Most notably, the opening of the binding pocket leads to the loss of three contacts with the  $\beta_1$ - $\beta_2$  loop and the gain of two contacts with the  $\beta_5$ - $\alpha_2$  loop. Together with several cases involving the strands  $\beta_2$ ,  $\beta_3$ ,  $\beta_5$ , and  $\beta_6$ , these contact changes lead to an overall compaction of the hydrophobic core of PDZ2S-trans, which is also reflected in the distributions of the radius of gyration (Figure 6F). The rigidity of these  $\beta$  sheets, particularly of  $\beta_6$ , however, seems to hamper the direct propagation of the  $\alpha_2$  conformational change to the C-terminus.

The other anchor residue of the photoswitch, Cys-21, is a part of the short  $\beta_2$ -strand of PDZ2S.  $\beta_2$  itself undergoes only minor changes [i.e., with respect to its secondary structure (Figure 5) and through the forming and breaking of one contact with  $\alpha_2$ , respectively]. In the N-terminal direction, the opening of the binding pocket at Cys-21 leads to a major structural rearrangement of the adjacent  $\beta_1$ - $\beta_2$  loop. That is, five out of its seven residues change their backbone dihedral angles (Table S5, Figure S7 of the Supporting Information), several contacts with the  $\alpha_2$ -helix and the  $\alpha_2$ - $\beta_6$  loop are destabilized, two intraloop contacts change, and a new backbone H bond is formed (Table 1). Overall, this leads to a stabilization of the  $\beta_1$ - $\beta_2$  loop, which is reflected in the significant narrowing of its conformational distribution (Figure 6C). The adjacent  $\beta_1$ -strand, on the other hand, is a part of the rather rigid  $\beta$  sheet scaffold of PDZ2S and therefore shows hardly any changes of its conformation or contacts. Similarly, the N-terminal region changes only little (e.g., by an overall decrease of the average number of contacts of 0.22), which leads to increased backbone fluctuations (Figure 4).

In the C-terminal direction, the opening of the binding pocket at Cys-21 leads to a significant conformational rearrangement of the adjacent  $\beta_2$ - $\beta_3$  loop. That is, eight out of its 11 residues change their backbone dihedral angles (Table S5 and Figures S8 and S9 of the Supporting Information), a contact with the  $\beta_5$ - $\alpha_2$  loop is formed, and an intraloop contact is lost. Interestingly, the conformational changes of  $\beta_2$ - $\beta_3$  move the loop toward the C-terminal loop, which yields two new contacts between the two loops. Moreover, the C-terminal loop forms a contact with the  $\beta_3$ -strand and two contacts with the  $\alpha_1$ - $\beta_4$  loop. These interactions lead to a stabilization of the C-terminal region, which is illustrated by the distribution of the distance between residues Val-30 and Pro-95 (Figure 6D) and the distribution of the end-to-end distance  $d_{91,94}$  of the C-terminal loop (Figure 6E).

It is interesting to discuss the above findings in the context of allosteric communication within a protein. Allostery is commonly explained as a change in the binding behavior of a distant active site subsequent to the binding of a ligand to an allosteric site. In their natural environment, PDZ domains are a part of a multidomain protein and take over the role of an allosteric site, while the active site is typically on another domain. As such, PDZ domains represent only “half” of an allosteric system. It has nevertheless been argued that the PDZ2 domain studied here does possess allosteric properties, even when looked at it as an isolated system (see ref 11). That is, a



PDZ domain in a multidomain protein must still “communicate” somehow with the other domain, to which it is linked and which carries an active site. In a looser sense, that communication can still be called allostery. However, it is not at all clear how that communication works, other than saying that communication must be related to the structural or dynamical properties of the parts of a PDZ domain which connect to other domains, either through a covalent link at the C-terminus or through the interface which associates to another domain. Hence, in a loose sense, we might call that interface the active site of the allosteric system. It is the goal of the present work, in connection with its experimental counterpart,<sup>45</sup> to address possible mechanisms of that communication.

In practice, this general definition is however complicated by the fact that a large variety of binding partners and schemes exist for both sites in typical allosteric systems. For example, in the PSD-95 protein, three connected PDZ domains are followed by a SH3 domain and a guanylate kinase domain.<sup>20</sup> Nevertheless, there are examples for which a relatively well-defined mechanism can be identified, such as in recent NMR experiments by Petit et al.<sup>13</sup> for PDZ3. They showed that the affinity of ligand-binding in PDZ3 is indeed directly related to the conformational motion of a small additional  $\alpha$ -helix attached to the C-terminus. That is, the removal of this helix affects an entropic change of the binding free energy such that the ligand affinity reduces by 21-fold.

In the case of PDZ2S, we find that the cis–trans isomerization of the photoswitch mimicking ligand binding induces significant changes of the conformational distribution and dynamics of the distant C-terminal region. Similar to the additional  $\alpha$ -helix that packs up against the core domain of PDZ3,<sup>13</sup> the C-terminal loop of PDZ2S was found to form several contacts with the  $\beta_2$ – $\beta_3$  loop and the  $\alpha_1$ – $\beta_4$  loop (Table 1). As a consequence, the distribution of the end-to-end distance  $d_{91,94}$  of the C-terminal loop (Figure 6E) changes in a specific manner. We note that the motion of the  $\beta_2$ – $\beta_3$  loop toward the C-terminal loop directly accounts for the motion along the first principal component (Figure 3).

## CONCLUSION

We have performed comprehensive MD simulations of the photoswitchable protein PDZ2S in its cis and trans states and the corresponding wild-type protein PDZ2 in its free and bound state. First we have calculated the experimentally deduced backbone dihedral angles and NOEs and found overall good agreement of simulation and experiment (Tables S2–S4 of the Supporting Information). Hence, our theoretical model (Amber99sb\*–ILDN and TIP3P, in total 14  $\mu$ s for PDZ2S) seems to be valid and sufficient to describe this quite flexible allosteric system.

In a second step, we have studied to what extent the cis–trans isomerization of the azobenzene photoswitch in PDZ2S indeed emulates the effects of peptide binding in PDZ2. Compared to the wild-type PDZ2 system, PDZ2S seems to be somewhat destabilized by the photoswitch. This is suggested by the larger conformational heterogeneity (Figure 3), the higher residue fluctuations (Figure 4), and (in cis only) the partial loss of structure-stabilizing H bonds in the  $\alpha_2$ -helix and the  $\beta_1$ – $\beta_2$  loop (Figure 5). On the other hand, recent melting experiments have revealed a slightly higher thermal stability of the photoswitched versus the wild-type system, which indicates an entropic stabilization of PDZ2S.<sup>70</sup> The initial conformational change caused by the cis–trans photoisomerization is certainly

larger than the local rearrangement of the wild-type system due to binding. Also, the subsequent propagation of the structural perturbation of the two systems agrees only in its overall trends (Figure 6 and Figure S5 of the Supporting Information). Given the unique potential of the photoswitchable system to study the conformational dynamics in real time, however, we feel that the photoswitchable system is per se an interesting and worthwhile system to study.

Following the validation of the theoretical model as well as the experimental concept of a photoswitchable allosteric protein, we have presented a detailed description of the conformational rearrangement of PDZ2S subsequent to cis–trans photoisomerization. In short, at the  $\alpha_2$ -side of the photoswitch, we observe an overall stabilization of the  $\alpha_2$ -helix, which involves the change of four H bonds and 13 further residue–residue contacts. At the  $\beta_2$ -side, the opening of the binding pocket leads to a major structural rearrangement of the two adjacent loops  $\beta_1$ – $\beta_2$  and  $\beta_2$ – $\beta_3$ , which is reflected in changes of the corresponding backbone dihedral angles as well as numerous changes of contacts. Most importantly, this rearrangement leads the formation of in total five contacts of  $\beta_2$ – $\beta_3$ ,  $\beta_3$ , and  $\alpha_1$ – $\beta_4$  with the C-terminal loop, which results in an overall stabilization of the C-terminal region. In the absence of a specific binding partner at the distant site, we consider this change of the conformational distribution and dynamics of the C-terminal region as the “allosteric response” of the isolated PDZ2S model system.

It is interesting to relate our findings to previous descriptions of the allosteric communication in PDZ domains. For example, a number of network models have been proposed that may reflect the intramolecular signal propagation. This includes networks based on the statistical analysis of evolutionary conserved sequences,<sup>30,31</sup> on vibrational energy flow,<sup>32,33</sup> or residue–residue interaction energies,<sup>34,35</sup> on  $C_\alpha$ – $C_\alpha$  correlations of low-frequency normal modes,<sup>36</sup> on the linear response to residue perturbation,<sup>37,38</sup> on coupled side-chain fluctuations,<sup>39</sup> on a force distribution analysis,<sup>40</sup> and on information-theoretical approaches.<sup>41–43</sup> In the present paper, we take yet another approach (i.e., we calculate the response of an allosteric protein upon a reasonably well-defined structural perturbation at its allosteric site). While the overall construct might appear artificial, it has the advantage that it can be tested against experiment in the long run. Several of the previous studies<sup>30,32,34</sup> indicated an allosteric pathway in PDZ2 that starts from the  $\alpha_2$ -helix and propagates via  $\beta_2$  and  $\beta_1$ – $\beta_2$  to the  $\alpha_1$ -helix (i.e., “across the upper part” of the PDZ domain in Figure 1), which, qualitatively speaking, is also the regions for which we observe the largest structural changes between the two states of the photoswitch. Naturally, it is per se not clear to what extent the various models account for allosteric effects because so far the different experimental and theoretical approaches cannot be compared directly. As a first step in this direction, we now perform extensive nonequilibrium MD studies of PDZ2S, which amount to a direct simulation of the time-resolved infrared experiments of Buchli et al. While the photoswitchable PDZ domain represents a simplified model of allostery, it may facilitate the direct comparison of time-resolved experiments and simulations.

## ASSOCIATED CONTENT

### Supporting Information

The sequence of PDZ2S, details on the MD methods, time evolution of the rmsd, table and Ramachandran plots of

residues that deviate in MD and the experiment, comparison of secondary structures in MD and the experiment, table of violations of long-range NOEs, distance distributions and Ramachandran plots of residues that change significantly as a consequence of ligand binding by PDZ2, and a PCA of the individual trajectories of PDZ2S-cis and PDZ2S-trans. This material is available free of charge via the Internet at <http://pubs.acs.org>.

## AUTHOR INFORMATION

### Corresponding Author

\*E-mail: [stock@physik.uni-freiburg.de](mailto:stock@physik.uni-freiburg.de).

### Notes

The authors declare no competing financial interest.

## ACKNOWLEDGMENTS

We thank Florian Sittel, Jonas Bartz, Brigitte Buchli, Steven A. Waldauer, Oliver Zerbe, Francesco Rao, Alan E. Mark, and Oliver Lange for numerous instructive and helpful discussions. This work has been supported by the Deutsche Forschungsgemeinschaft to G.S. as well as by an Advanced Investigator ERC grant (DYNALLO) to P.H.

## REFERENCES

- (1) Nussinov, R.; Tsai, C.-J. Allostery in Disease and in Drug Discovery. *Cell* **2013**, *153*, 293–305.
- (2) Motlagh, H. N.; Wrabl, J. O.; Li, J.; Hilser, V. J. The Ensemble Nature of Allostery. *Nature (London)* **2014**, *508*, 331–339.
- (3) Monod, J.; Wyman, J.; Changeux, J.-P. On the Nature of Allosteric Transitions: A Plausible Model. *J. Mol. Biol.* **1965**, *12*, 88–118.
- (4) Cui, Q.; Karplus, M. Allostery and Cooperativity Revisited. *Protein Sci.* **2008**, *17*, 1295–1307.
- (5) Cooper, A.; Dryden, D. Allostery without Conformational Change: A Plausible Model. *Eur. Biophys. J. Biophys. Lett.* **1984**, *11*, 103–109.
- (6) Kern, D.; Zuiderweg, E. The Role of Dynamics in Allosteric Regulation. *Curr. Opin. Struct. Biol.* **2003**, *13*, 748–757.
- (7) Popovych, N.; Sun, S.; Ebright, R. Kalodimos, Dynamically Driven Protein Allostery. *Nat. Struct. Mol. Biol.* **2006**, *13*, 831–838.
- (8) Frederick, K. K.; Marlow, M. S.; Valentine, K. G.; Wand, A. J. Conformational Entropy in Molecular Recognition by Proteins. *Nature* **2007**, *448*, 325–329.
- (9) Smock, R. G.; Gierasch, L. M. Sending Signal Dynamically. *Science* **2009**, *324*, 198–203.
- (10) Dhulesia, A.; Gsponer, J.; Vendruscolo, M. Mapping of Two Networks of Residues that Exhibit Structural and Dynamical Changes upon Binding in a PDZ Domain Protein. *J. Am. Chem. Soc.* **2008**, *130*, 8931–8939.
- (11) Fuentes, E.; Der, C.; Lee, A. Ligand-Dependent Dynamics and Intramolecular Signaling in a PDZ Domain. *J. Mol. Biol.* **2004**, *335*, 1105–1115.
- (12) Fuentes, E. J.; Gilmore, S. A.; Mauldin, R. V.; Lee, A. L. Evaluation of Energetic and Dynamic Coupling Networks in a PDZ Domain Protein. *J. Mol. Biol.* **2006**, *364*, 337–351.
- (13) Petit, C. M.; Zhang, J.; Sapienza, P. J.; Fuentes, E. J.; Lee, A. L. Hidden Dynamic Allostery in a PDZ Domain. *Proc. Natl. Acad. Sci. U.S.A.* **2009**, *106*, 18249–18254.
- (14) Cilia, E.; Vuister, G. W.; Lenaerts, T. Accurate Prediction of the Dynamical Changes within the Second PDZ Domain of PTP1e. *PLoS Comput. Biol.* **2012**, *8*.
- (15) Doyle, D.; Lee, A.; Lewis, J.; Kim, E.; Sheng, M.; MacKinnon, R. Crystal Structures of a Complexed and Peptide-Free Membrane Protein-Binding Domain: Molecular Basis of Peptide Recognition by PDZ. *Cell* **1996**, *85*, 1067–1076.
- (16) Zhang, J.; Sapienza, P. J.; Ke, H.; Chang, A.; Hengel, S. R.; Wang, H.; Phillips, G. N., Jr.; Lee, A. L. Crystallographic and Nuclear Magnetic Resonance Evaluation of the Impact of Peptide Binding to the Second PDZ Domain of Protein Tyrosine Phosphatase 1E. *Biochemistry* **2010**, *49*, 9280–9291.
- (17) Chi, C. N.; Bach, A.; Stromgaard, K.; Gianni, S.; Jemth, P. Ligand Binding by PDZ Domains. *Biofactors* **2012**, *38*, 338–348.
- (18) Harris, B.; Lim, W. Mechanism and Role of PDZ Domains in Signaling Complex Assembly. *J. Cell Sci.* **2001**, *114*, 3219–3231.
- (19) van Ham, M.; Hendriks, W. PDZ Domains: Glue and Guide. *Mol. Biol. Rep.* **2003**, *30*, 69–82.
- (20) Lee, H.-J.; Zheng, J. J. PDZ Domains and their Binding Partners: Structure, Specificity, and Modification. *Cell Commun. Signal.* **2010**, *8*.
- (21) Leitner, D.; Straub, J. *Proteins: Energy, Heat and Signal Flow*; Taylor and Francis/CRC Press: London, 2009.
- (22) Nguyen, P. H.; Derreumaux, P.; Stock, G. Energy Flow and Long-Range Correlations in Guanine-Binding Riboswitch: A Non-equilibrium Molecular Dynamics Study. *J. Phys. Chem. B* **2009**, *113*, 9340–9347.
- (23) Hub, J. S.; Kubitzki, M.; de Groot, B. L. Spontaneous Quaternary and Tertiary T-R Transitions of Human Hemoglobin in Molecular Dynamics Simulation. *PLoS Comput. Biol.* **2010**, *6*, e1000774.
- (24) Gnanasekaran, R.; Agbo, J. K.; Leitner, D. M. Communication Maps Computed for Homodimeric Hemoglobin: Computational Study of Water-Mediated Energy Transport in Proteins. *J. Chem. Phys.* **2011**, *135*, 065103.
- (25) Elber, R. Simulations of Allosteric Transitions. *Curr. Opin. Struct. Biol.* **2011**, *21*, 167–172.
- (26) Vesper, M. D.; de Groot, B. L. Collective Dynamics Underlying Allosteric Transitions in Hemoglobin. *PLoS Comp. Biol.* **2013**, *9*, e1003232.
- (27) McLeish, T. C. B.; Rodgers, T. L.; Wilson, M. R. Allostery without Conformational Change: Modelling Protein Dynamics at Multiple Scales. *Phys. Biol.* **2013**, *10*, 056004.
- (28) Rodgers, T. L.; Townsend, P. D.; Burnell, D.; Jones, M. L.; Richards, S. A.; McLeish, T. C. B.; Pohl, E.; Wilson, M. R.; Cann, M. J. Modulation of Global Low-Frequency Motions Underlies Allosteric Regulation: Demonstration in CRP/FNR Family Transcription Factors. *PLoS Biol.* **2013**, *11*, e1001651.
- (29) Krukau, A.; Knecht, V.; Lipowsky, R. Allosteric Control of Kinesin's Motor Domain by Tubulin: A Molecular Dynamics Study. *Phys. Chem. Chem. Phys.* **2014**, *16*, 6189–6198.
- (30) Lockless, S. W.; Ranganathan, R. Evolutionarily Conserved Pathways of Energetic Connectivity in Protein Families. *Science* **1999**, *286*, 295–299.
- (31) Chi, C. N.; Elfstrom, L.; Shi, Y.; Snall, T.; Engstrom, A.; Jemth, P. Reassessing a Sparse Energetic Network within a Single Protein Domain. *Proc. Natl. Acad. Sci. U.S.A.* **2008**, *105*, 4679–4684.
- (32) Ota, N.; Agard, D. A. Intramolecular Signaling Pathways Revealed by Molecular Anisotropic Thermal Diffusion. *J. Mol. Biol.* **2005**, *351*, 345–354.
- (33) Sharp, K.; Skinner, J. J. Pump-Probe Molecular Dynamics as a Tool for Studying Protein Motion and Long Range Coupling. *Proteins* **2006**, *65*, 347–361.
- (34) Kong, Y.; Karplus, M. Signaling Pathways of PDZ2 Domain: A Molecular Dynamics Interaction Correlation Analysis. *Proteins* **2009**, *74*, 145–154.
- (35) S.Vijayabaskar, M.; Vishveshwara, S. Interaction Energy Based Protein Structure Networks. *Biophys. J.* **2010**, *99*, 3704–3715.
- (36) De Los Rios, P.; Cecconi, F.; Pretre, A.; Dietler, G.; Michielin, O.; Piazza, F.; Juanico, B. Functional Dynamics of PDZ Binding Domains: A Normal-Mode Analysis. *Biophys. J.* **2005**, *89*, 14–21.
- (37) Gereke, Z. N.; Keskin, O.; Ozkan, S. B. Identification of Specificity and Promiscuity of PDZ Domain Interactions through their Dynamic Behavior. *Proteins* **2009**, *77*, 796–811.



- (38) Gerek, Z. N.; Ozkan, S. B. Change in Allosteric Network Affects Binding Affinities of PDZ Domains: Analysis through Perturbation Response Scanning. *PLoS Comput. Biol.* **2011**, *7*, e1002154.
- (39) Bowman, G. R.; Geissler, P. L. Equilibrium Fluctuations of a Single Folded Protein Reveal a Multitude of Potential Cryptic Allosteric Sites. *Proc. Natl. Acad. Sci. U.S.A.* **2012**, *109*, 11681–11686.
- (40) Stacklies, W.; Xia, F.; Gräter, F. Dynamic Allostery in the Methionine Repressor Revealed by Force Distribution Analysis. *PLoS Comput. Biol.* **2009**, *5* (e1000574), 11.
- (41) Chennubhotla, C.; Bahar, I. Signal Propagation in Proteins and Relation to Equilibrium Fluctuations. *PLoS Comput. Biol.* **2007**, *9* (e172), 1716–1726.
- (42) Pandini, A.; Fornili, A.; Fraternali, F.; Kleinjung, J. Detection of Allosteric Signal Transmission by Information-Theoretic Analysis of Protein Dynamics. *FASEB J.* **2012**, *26*, 868–881.
- (43) LeVine, M. V.; Weinstein, H. NBIT: A New Information Theory-Based Analysis of Allosteric Mechanisms Reveals Residues that Underlie Function in the Leucine Transporter LeuT. *PLoS Comput. Biol.* **2014**, *10*, e1003603.
- (44) Assignments are from MOLMOL (ref 71), based on the NMR structure of PDZ2S-cis.
- (45) Buchli, B.; Waldauer, S. A.; Walser, R.; Donten, M. L.; Pfister, R.; Bloechli, N.; Steiner, S.; Cafilisch, A.; Zerbe, O.; Hamm, P. Kinetic Response of a Photoperturbed Allosteric Protein. *Proc. Natl. Acad. Sci. U.S.A.* **2013**, *110*, 11725–11730.
- (46) Kumita, J. R.; Smart, O. S.; Woolley, G. A. Photo-Control of Helix Content in a Short Peptide. *Proc. Natl. Acad. Sci. U.S.A.* **2000**, *97*, 3803–3808.
- (47) Renner, C.; Moroder, L. Azobenzene as Conformational Switch in Model Peptides. *Chem. Biol. Chem.* **2006**, *7*, 869–878.
- (48) Bredenbeck, J.; Helbing, J.; Sieg, A.; Schrader, T.; Zinth, W.; Renner, C.; Behrendt, R.; Moroder, L.; Wachtveitl, J.; Hamm, P. Picosecond Conformational Transition and Equilibration of a Cyclic Peptide. *Proc. Natl. Acad. Sci. U.S.A.* **2003**, *100*, 6452–6457.
- (49) Volgraf, M.; Gorostiza, P.; Numano, R.; Kramer, R. H.; Isacoff, E. Y.; Trauner, D. Allosteric Control of an Ionotropic Glutamate Receptor with an Optical Switch. *Nat. Chem. Biol.* **2006**, *2*, 47–52.
- (50) Numano, R.; Szobota, S.; Lau, A. Y.; Gorostiza, P.; Volgraf, M.; Roux, B.; Trauner, D.; Isacoff, E. Y. Nanosculpting Reversed Wavelength Sensitivity into a Photoswitchable iGluR. *Proc. Natl. Acad. Sci. U.S.A.* **2009**, *106*, 6814–6819.
- (51) Nguyen, P. H.; Staudt, H.; Wachtveitl, J.; Stock, G. Real Time Observation of Ultrafast Peptide Conformational Dynamics: MD Simulation vs. IR Experiment. *J. Phys. Chem. B* **2011**, *115*, 13084–13092.
- (52) Pronk; et al. GROMACS 4.5: a High-Throughput and Highly Parallel Open Source Molecular Simulation Toolkit. *Bioinformatics* **2013**, *29*, 845–854.
- (53) Hornak, V.; Abel, R.; Okur, A.; Strockbine, B.; Roitberg, A.; Simmerling, C. Comparison of Multiple Amber Force Fields and Development of Improved Protein Backbone Parameters. *Proteins* **2006**, *65*, 712–725.
- (54) Best, R. B.; Hummer, G. Optimized Molecular Dynamics Force Fields Applied to the Helix-Coil Transition of Polypeptides. *J. Phys. Chem. B* **2009**, *113*, 9004–9015.
- (55) Lindorff-Larsen, K.; Piana, S.; Palmo, K.; Maragakis, P.; Klepeis, J. L.; Dror, R. O.; Shaw, D. E. Improved Side-Chain Torsion Potentials for the Amber ff99SB Protein Force Field. *Proteins* **2010**, *78*, 1950–1958.
- (56) Jorgensen, W. L.; Chandrasekhar, J.; Madura, J. D.; Impey, R. W.; Klein, M. Comparison of Simple Potential Functions for Simulating Liquid Water. *J. Chem. Phys.* **1983**, *79*, 926.
- (57) Joung, I. S.; Cheatham, T. E., III Determination of Alkali and Halide Monovalent Ion Parameters for Use in Explicitly Solvated Biomolecular Simulations. *J. Phys. Chem. B* **2008**, *112*, 9020–9041.
- (58) Frisch, M. J. et al. *Gaussian 09*, revision A.1; Gaussian Inc: Wallingford, CT, 2009.
- (59) Bayly, C. I.; Cieplak, P.; Cornell, W. D.; Kollman, P. A. A Well-Behaved Electrostatic Potential Based Method Using Charge Restraints for Deriving Atomic Charges: The RESP Model. *J. Phys. Chem.* **1993**, *97*, 10269–10280.
- (60) Wang, J.; Wang, W.; Kollman, P. A.; Case, D. A. Antechamber, An Accessory Software Package for Molecular Mechanical Calculations. *J. Comput. Chem.* **2005**, *25*, 1157–1174.
- (61) Hess, B.; Kutzner, C.; van der Spoel, D.; Lindahl, E. GROMACS 4: Algorithms for Highly Efficient, Load-Balanced, and Scalable Molecular Simulation. *J. Chem. Theor. Comp.* **2008**, *4*, 435–447.
- (62) Darden, T.; York, D.; Petersen, L. Particle mesh Ewald: An  $N \log(N)$  Method for Ewald Sums in Large Systems. *J. Chem. Phys.* **1993**, *98*, 10089–10092.
- (63) Bussi, G.; Donadio, D.; Parrinello, M. Canonical Sampling through Velocity Rescaling. *J. Chem. Phys.* **2007**, *126*, 0141011–0141017.
- (64) Berendsen, H. J. C.; Postma, J. P. M.; van Gunsteren, W. F.; Dinola, A.; Haak, J. R. Molecular Dynamics with Coupling to an External Bath. *J. Chem. Phys.* **1984**, *81*, 3684–3690.
- (65) Shen, Y.; Delaglio, F.; Cornilescu, G.; Bax, A. TALOS Plus: A Hybrid Method for Predicting Protein Torsion Angles from NMR Chemical Shifts. *J. Biomol. NMR* **2009**, *44*, 213–223.
- (66) Altis, A.; Nguyen, P. H.; Hegger, R.; Stock, G. Dihedral Angle Principal Component Analysis of Molecular Dynamics Simulations. *J. Chem. Phys.* **2007**, *126*, 244111.
- (67) Kabsch, W.; Sander, C. Dictionary of Protein Secondary Structure: Pattern Recognition of Hydrogen Bonded and Geometrical Features. *Biopolymers* **1983**, *22*, 2577–2637.
- (68) Fan, H.; Mark, A. E. Relative Stability of Protein Structures Determined by X-ray Crystallography or NMR Spectroscopy: A Molecular Dynamics Simulation Study. *Proteins* **2003**, *53*, 111–120.
- (69) Amadei, A.; Linssen, A. B. M.; Berendsen, H. J. C. Essential Dynamics of Proteins. *Proteins* **1993**, *17*, 412–425.
- (70) Waldauer, S. A.; Stucki-Buchli, B.; Frey, L.; Hamm, P. Effect of Viscogens on the Kinetic Response of a Photoperturbed Allosteric Protein. *J. Chem. Phys.* **2014**, *141*, 22D514.
- (71) Koradi, R.; Billeter, M.; Wüthrich, K. Molmol: A Program for Display and Analysis of Macromolecular Structures. *J. Mol. Graphics* **1996**, *14*, 51–55.